Inorganic Chemistry

Article

pubs.acs.org/IC

Visible to Near-Infrared Emission from Ln^{III}(Bis-oxazoline)–$[Mo^{V}(CN)_8]$ (Ln = Ce–Yb) Magnetic Coordination Polymers Showing Unusual Lanthanide-Dependent Sliding of Cyanido-Bridged Layers

Szymon Chorazy,[‡,†] Mirosław Arczynski,[†] Koji Nakabayashi,[‡] Barbara Sieklucka,*[,†] and Shin-ichi Ohkoshi*[,‡,#]

[‡]Department of Chemistry, School of Science, The University of Tokyo, 7-3-1 Hongo, Bunkyo-ku, Tokyo 113-0033, Japan

[†]Faculty of Chemistry, Jagiellonian University, Ingardena 3, 30-060 Krakow, Poland

[#]CREST, JST, K's Gobancho, 7 Gobancho, Chiyoda-ku, Tokyo 102-0076, Japan

Supporting Information

ABSTRACT: Complexes of lanthanides(III) (Ce–Yb) with 2,2′-bis(2-oxazoline) (Box) combined with octacyanidomolybdate(V) gave a series of magneto-luminescent coordination polymers, $\{[Ln^{III}(Box)_n(DMF)_m][Mo^{V}(CN)_8]\}\cdot x$(solvent) (**1**–**12**). They are built of cyanido-bridged layers of a mixed 4- and 8-metal rings topology and show unique sliding of layers dependent on a 4f metal ion. For light lanthanides, dominant phase A, $\{[Ln^{III}(Box)_2(DMF)_2][Mo^{V}(CN)_8]\}\cdot 1.5MeCN$ (Ln = Ce, **1**; Pr, **2**; Nd, **3**), consists of ideally aligned, not shifted layers, giving large channels (13.7 × 14.0 Å). Intermediate lanthanides reveal phase B, $\{[Ln^{III}(Box)_2(DMF)_2][Mo^{V}(CN)_8]\}\cdot H_2O$ (Ln = Sm, **4**; Eu, **5**; Gd, **6**; Tb, **7**; Dy, **8**), of smaller pores (8.4 × 10.6 Å) due to layer-H_2O hydrogen bonding, which induces sliding of CN^--bridged layers. Heavy lanthanides show phase C, $\{[Ln^{III}(Box)(DMF)_3][Mo^{V}(CN)_8]\}\cdot MeCN$ (Ln = Ho, **9**; Er, **10**; Tm, **11**; Yb, **12**), with large channels (13.7 × 13.7 Å) of a similar size to light lanthanides. This effect comes from the changes in Ln^{III} coordination sphere affecting solvent–layer interactions. Compounds **1**–**12** reveal diverse emission depending on the interaction between Ln^{III} and Box luminophors. For **2**–**5**, **9**, and **12**, the ligand-to-metal energy-transfer-induced visible f-centered emission ranging from green for Ho^{III}-based **9**, orange from Sm^{III}-based **4**, to red for Pr^{III}- and Eu^{III}-containing **2** and **5**, respectively. Near-infrared emission was found for **2**–**4**, **9**, and **12**. Red phosphorescence of Box was detected for Gd^{III}-based **6**, whereas the selective excitation of ligand or Ln^{III} excited states resulting in the switchable red to green emission was found for Tb^{III}-based **7**. The materials revealed Ln^{III}–Mo^{V} magnetic coupling leading to ferromagnetism below 2.0 and 2.2 K for **4** and **7**, respectively. The onset of magnetic ordering at low temperatures was found for **6** and **8**. Compounds **1**–**12** form a unique family of cyanido-bridged materials of a bifunctional magneto-luminescence character combined with dynamic structural features.

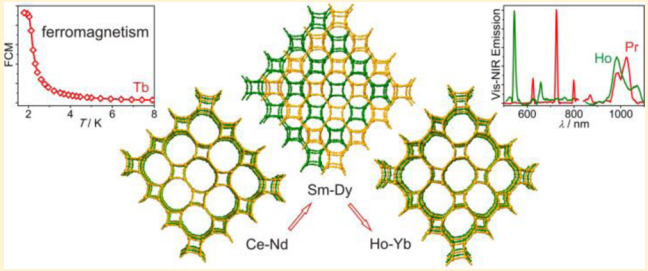

INTRODUCTION

Multifunctional materials, combining at least two magnetic, electrical, or optical properties, are of a special interest as they serve as promising prerequisites for the application in information storage, selective sensing, and construction of fast, economical electronic devices.[1−6] In this regard, the great effort is focused on the synthesis of molecular magnets which are built of magnetically active complexes of metal ions, or organic radicals. They differ from the metal- or metal-oxides-based magnets as their structure, and resulting properties, can be designed by the choice of building blocks, selected from an unlimited set of organic/inorganic molecules.[7,8] Molecular magnets can reveal not only exchange interaction leading to magnetic ordering below critical temperature (T_c)[9,10] but also unique effect of slow magnetic relaxation giving the magnetic hysteresis of a single molecule origin.[11,12] Moreover, these properties can be combined with other functionalities, such as ferroelectricity,[13,14] sensitivity to guest molecules,[15−17] chirality,[18,19] or luminescence.[20−23]

The properties implemented into a multifunctional material can coexist, modify each other, or interact giving a cross-effect.[19] The spectacular phenomena are induced when the introduced property is combined with magnetic ordering. It opened remarkable families of conductive magnets,[24,25] molecular multiferroics,[13] and magnetic sponges with T_c triggered by dehydration.[15,17] Among others, the conjunction of magnetism with optical properties was shown to be fruitful. Chirality combined with magnetic ordering lead to a cross-effect of magneto-chiral dichroism enhanced below T_c as shown for oxalate-bridged Mn^{II}–Cr^{III} (T_c = 7 K) ferromagnet with chiral counterion.[26] Enantiopure magnets reveal natural (NCD) and magnetic circular dichroism (MCD), with the enhancement of

Received: January 7, 2015
Published: May 6, 2015

DOI: 10.1021/acs.inorgchem.5b00040
Inorg. Chem. 2015, 54, 4724–4736

MCD below T_c, as proved for CN^--bridged $Mn^{II}(L)-Nb^{IV}$ (T_c = 23.5 K, L = α-methyl-2-pyridine methanol) ferrimagnet.[27] Second harmonic generation (SHG) is also modulated when combined with magnetic ordering. The related effect of magnetization-induced SHG was presented in both selected oxalate- and cyanido-bridged molecular magnets.[28,29] Particular attention is paid to photomagnetic materials which can switch between two or more magnetic states by light irradiation, and even the switchability between the nonmagnetized and magnetically ordered state can be found. Such a light-induced magnet is realized by the induction of charge transfer in bimetallic assemblies built of 3d metal ions and cyanidometallates.[30−32] The alternative way is based on light-induced spin-crossover as shown for octacyanido-based $Fe^{II}(L)-Nb^{IV}$ (L = 4-pyridinealdoxime) photomagnet.[33] Using this approach, we prepared a first chiral $Fe^{II}(L)-Nb^{IV}$ (L = 4-bromopyridine) photomagnet, and a cross-effect of 90° optical switching of output SHG was detected.[34]

A great potential lies also in emissive molecular magnets combining magnetic ordering with luminescence, which are an alternative to luminescent magnetic nanocomposites built of fluorescent quantum dots bounded with magnetic nanoparticles.[35] In contrast to these materials, for which emission and magnetism originate from two independent ingredients, emissive molecular magnets are intrinsically both emissive and magnetic.[21,22] It gives the opportunity to detect a diversity of luminescent effects in a magnetic system and the coupling between both properties. However, magnetic ordering with emission were found only for a small group of molecular materials, consisting of a carboxylate-bridged Ni^{II} network (T_c = 9.5 K, ligand emission),[36] cyanido-bridged $Tb^{III}-W^V$ ferromagnets (T_c = 2.8 K, Tb^{III} emission; T_c = 2.4 K, Tb^{III} and ligand emission),[20,21] as well as oxamato-bridged $Co^{II}-Cu^{II}$ (T_c = 19 K, emission of Ru^{II}-based counterion),[37] and $Mn^{II}-Cu^{II}$ (T_c = 19 K, luminescent organic counterion) magnets.[38]

All these examples show an increasing interest in functional molecular magnets, especially of a magneto-optical character. However, the main effort is focused on searching for single novel materials with exceptional functionalities. Although this approach ensures scientific progress, the absence of reports on systematic work disallows the understanding of multifuctionalities and a selection of the best building blocks for the enhancement of desired properties. We thus have undertaken the challenge of systematic studies of magneto-optical functionalities in molecular magnets, starting from the luminescence combined with magnetic properties. We selected coordination assemblies based on lanthanides(III) and paramagnetic octacyanidometallates, offering eight cyanides for mediating in magnetic interactions, which often leads to magnetic ordering. They are not emissive but do not absorb the visible and near-infrared light, thereby allowing the observation of luminescence from other building blocks.[20,21] Most of the lanthanide(III) ions are paramagnetic, and they often reveal magnetic anisotropy, inducing unusual magnetic properties[39] alone and in combination with $[M(CN)_8]^{n-}$ ions.[40] Most lanthanides(III) are emissive in either the visible or near-infrared range, and they show a variety of luminescent effects, including strong interaction with ligands serving as an antenna for enhanced f-centered emission.[41] The family of paramagnetic lanthanides(III) consists of 12 members, and their reactivity is very similar, so a broad series can be investigated in details. However, due to the increasing ionic radius, their reactivity can change, going from light to heavy lanthanides, which affects the structural features and properties. This effect was found in a series of Ln^{III}(2,2′:6′,2″-terpyridine)−W^V systems changing from chains for Ce−Dy, to dinuclear molecules for Ho−Yb.[42]

At the current time, only a few magneto-luminescent materials based on a 4f metal and $[M(CN)_8]^{3-}$ (M = Mo, W) have been reported. The visible Tb^{III} and Eu^{III} emission was found for $\{[M^{III}(H_2O)_5][M^V(CN)_8]\}$ (M^{III} = Eu, Tb; Eu−Gd, Eu−Tb, Tb−Sm = 1:1; M = Mo, W) 2-D magnets,[21,43] whereas NIR luminescence was presented in Nd^{III}(1,10-phenanthroline)−Mo/W^V chains bearing ferromagnetic coupling.[44] We have shown a pair of enantiopure Eu^{III}(iPr-Pybox)−W^V (iPr-Pybox = 2,6-bis(4-isopropyl-2-oxazolin-2-yl)pyridine) helical chains revealing chirality, paramagnetism, and thermally switchable luminescence.[45] Later, the chiral helices of $Nd^{III}-W^V$ and $Gd^{III}-W^V$ have been characterized, and they showed ferromagnetic coupling with Nd^{III}-based near-infrared emission and antiferromagnetic coupling with red ligand phosphorescence, respectively.[46] The interesting magnetic properties, including magnetic ordering,[47] have been also found for other $Ln^{III}-[M(CN)_8]$ systems, but their emission has not been examined.

More importantly, we have recently reported a cyanido-bridged $Tb^{III}(L)-W^V$ (T_c = 2.4 K, L = 2,2′-bis(2-oxazoline)) layered ferromagnet showing a switchability between Tb^{III}-centered green and ligand-based red emission by using a different wavelength of excitation light.[20] It showed that combination of Ln^{III} with Box ligand and $[M^V(CN)_8]^{3-}$ resulted in magnetic interactions and ordering, coexisting with various emission properties coming from the interaction between f-metal and ligand excited states. Here, we follow these discoveries, and report the synthesis and detailed structural, optical and magnetic studies of a series of $\{[Ln^{III}(Box)_n(DMF)_m][Mo^V(CN)_8]\}\cdot x$(solvent) (Ln = Ce−Yb, **1**−**12**) layered materials combining Ln-dependent diversity of luminescent and magnetic phenomena, as well as unusual two-step sliding of cyanido-bridged layers.

EXPERIMENTAL SECTION

Materials. The tetrabutylammonium octacyanidomolybdate(V), $TBA_3[Mo^V(CN)_8]$ was synthesized according to the published procedure.[48] 2,2′-Bis(2-oxazoline) (Box), lanthanides(III) nitrates *n*-hydrates, and all solvents (acetonitrile = MeCN, *N*,*N*-dimethylformamide = DMF, diethyl ether = Et_2O) were purchased from Tokyo Chemical Industry or Wako Chemicals GmbH.

Syntheses and Basic Characterization of 1−12. To ensure a reliable comparison of reactivity, the same synthetic procedures were used for **1**−**12**. The *n*-hydrated lanthanide(III) nitrate (*n* = 4−6, 0.02 mmol) and 2,2′-bis(2-oxazoline) (8.4 mg, 0.06 mmol) were dissolved in 2.0 mL of MeCN, and the resulting solution was stirred for 5 min. Then, the portion of DMF (100 μL, 1.2 mmol) was added, and further stirring for 5 min was performed. After that, the solution of $TBA_3[Mo^V(CN)_8]$ (20.6 mg, 0.02 mmol) in 1.0 mL of MeCN was added. The resulting yellow solution was briefly stirred and layered by Et_2O (∼5.0 mL). After a few days, a reasonable amount of crystals appeared. The shape, color, and stability of the crystals upon exposure to the air depend on the lanthanide ion. For IR spectra and CHN analysis, the crystals were filtrated, washed by Et_2O, and dried in air. For the single-crystal X-ray experiment and other measurements, the crystals were protected from the contact with air in various ways, depending on the physical technique (see below).

*$[Ce^{III}(Box)_2(DMF)_2][Mo^V(CN)_8]\cdot 1.5MeCN$ (**1**).* The title compound was produced as yellowish green needle crystals. The formula was found from the X-ray diffraction experiment. After

DOI: 10.1021/acs.inorgchem.5b00040
Inorg. Chem. 2015, 54, 4724−4736

filtration, washing by Et_2O, and air-drying, **1** exchanges MeCN solvent into H_2O to give air-stable composition, $[Ce^{III}(Box)_2(DMF)_2]_2[Mo^V(CN)_8]_2{\cdot}3H_2O$ (formula taken from CHN analysis). Yield: 6.2 mg, 34%. IR (KBr, cm^{-1}). CN^- stretching vibrations: 2178w, 2172w, 2163m, 2152m, 2130w. Anal. Calcd for $Ce_1Mo_1C_{26}H_{36}N_{14}O_9$ (M_w = 924.7 g·mol^{-1}): C, 33.77%; H, 3.92%; N, 21.21%. Found: C, 33.64%; H, 4.01%; N, 21.10%. It is important to note that among the overwhelming amount of needle crystals, a few block crystals were observed. They are the second phase, $[Ce^{III}(Box)_2(DMF)_2]_2[Mo^V(CN)_8]_2{\cdot}H_2O$, analogous to that found for **2**–**8**. However, the quality of these crystals were poor, and attempts to characterize them by X-ray experiment were unsuccessful.

*$[Pr^{III}(Box)_2(DMF)_2][Mo^V(CN)_8]{\cdot}1.5MeCN$ (**2a**).* The title compound was produced as yellow needle crystals. The formula was taken from the results of X-ray diffraction experiment. Filtration, washing by Et_2O, and air-drying result in the exchange of solvent molecules of MeCN by H_2O, which gives the air-stable composition of **2a**, $[Pr^{III}(Box)_2(DMF)_2]_2[Mo^V(CN)_8]_2{\cdot}3H_2O$. Yield: 5.2 mg, 28%. IR (KBr, cm^{-1}). CN^- stretching vibrations: 2180w, 2173w, 2164m, 2152m, 2130w. Anal. Calcd for $Pr_1Mo_1C_{26}H_{36}N_{14}O_9$ (M_w = 925.5 g·mol^{-1}): C, 33.74%; H, 3.92%; N, 21.19%. Found: C, 33.45%; H, 4.11%; N, 20.93%.

*$[Pr^{III}(Box)_2(DMF)_2][Mo^V(CN)_8]{\cdot}H_2O$ (**2b**).* The title compound was produced as yellow block crystals. The formula was found from the results of X-ray diffraction experiment. This phase grows as a small impurity among the large amount of needle crystals of **2a**. Only the X-ray diffraction experiment was performed for **2b**. For other physical measurements, the properties of **2a** are presented. It was verified, however, that the physical properties of **2** are not noticeably affected by the variable amount of **2b**.

*$[Nd^{III}(Box)_2(DMF)_2][Mo^V(CN)_8]{\cdot}1.5MeCN$ (**3a**).* The title compound was produced as yellow needle crystals. The formula was found from the X-ray diffraction structural analysis. After filtration, washing by Et_2O, and air-drying, **3a** exchanges solvent molecules of MeCN into H_2O to give air-stable composition, $[Nd^{III}(Box)_2\ (DMF)_2]_2[Mo^V(CN)_8]_2{\cdot}3H_2O$. Yield: 6.1 mg, 33%. IR (KBr, cm^{-1}). CN^- stretching vibrations: 2181w, 2173w, 2165m, 2153m, 2127w. Anal. Calcd for $Nd_1Mo_1C_{26}H_{36}N_{14}O_9$ (M_w = 928.8 g·mol^{-1}): C, 33.62%; H, 3.91%; N, 21.11%. Found: C, 33.76%; H, 3.82%; N, 21.27%.

*$[Nd^{III}(Box)_2(DMF)_2][Mo^V(CN)_8]{\cdot}H_2O$ (**3b**).* The title compound was produced as yellow block crystals. The formula was found from the X-ray diffraction experiment. This phase grows as a small impurity among the large amount of needle crystals of **3a**. Only the X-ray diffraction structural analysis could be performed for **3b**. For other physical measurements, the properties of **3a** are shown. It was additionally confirmed that the physical properties of **3** are not noticeably affected by the variable amount of **3b**.

*$[Sm^{III}(Box)_2(DMF)_2][Mo^V(CN)_8]{\cdot}H_2O$ (**4**).* The title compound was produced as air-stable yellow block crystals. The formula found from the X-ray diffraction experiment is in a good agreement with the results of CHN analysis. Yield: 7.0 mg, 39%. IR (KBr, cm^{-1}). CN^- stretching vibrations: 2180m, 2170sh, 2167m, 2152m, 2135w. Anal. Calcd for $Sm_1Mo_1C_{26}H_{32}N_{14}O_7$ (M_w = 898.9 g·mol^{-1}): C, 34.74%; H, 3.59%; N, 21.81%. Found: C, 34.47%; H, 3.92%; N, 21.57%.

*$[Eu^{III}(Box)_2(DMF)_2][Mo^V(CN)_8]{\cdot}H_2O$ (**5**).* The title compound was produced as air-stable yellow block crystals. The formula taken from the X-ray diffraction experiment corresponds well with the results of CHN analysis. Yield: 6.5 mg, 36%. IR (KBr, cm^{-1}). CN^- stretching vibrations: 2179m, 2170sh, 2165m, 2152w, 2135w. Anal. Calcd for $Eu_1Mo_1C_{26}H_{32}N_{14}O_7$ (M_w = 900.5 g·mol^{-1}): C, 34.58%; H, 3.58%; N, 21.78%. Found: C, 34.24%; H, 3.71%; N, 21.64%.

*$[Gd^{III}(Box)_2(DMF)_2][Mo^V(CN)_8]{\cdot}H_2O$ (**6**).* The title compound was produced as air-stable yellow block crystals. The formula found from the X-ray diffraction experiment agrees well with the results of CHN analysis. Yield: 7.5 mg, 41%. IR (KBr, cm^{-1}). CN^- stretching vibrations: 2180m, 2171sh, 2167m, 2152w, 2136w. Anal. Calcd for $Gd_1Mo_1C_{26}H_{32}N_{14}O_7$ (M_w = 905.8 g·mol^{-1}): C, 34.47%; H, 3.56%; N, 21.65%. Found: C, 34.14%; H, 3.80%; N, 21.40%.

*$[Tb^{III}(Box)_2(DMF)_2][Mo^V(CN)_8]{\cdot}H_2O$ (**7**).* The title compound was produced as air-stable yellow block crystals. The formula found from the X-ray diffraction structural analysis agrees well with the results of CHN analysis. Yield: 6.2 mg, 34%. IR (KBr, cm^{-1}). CN^- stretching vibrations: 2181m, 2172sh, 2168m, 2152w, 2136vw. Anal. Calcd for $Tb_1Mo_1C_{26}H_{32}N_{14}O_7$ (M_w = 907.5 g·mol^{-1}): C, 34.41%; H, 3.55%; N, 21.61%. Found: C, 34.14%; H, 3.75%; N, 21.42%.

*$[Dy^{III}(Box)_2(DMF)_2][Mo^V(CN)_8]{\cdot}H_2O$ (**8**).* The title compound was produced as air-stable yellow block crystals. The formula found from the X-ray diffraction structural analysis agrees well with the results of CHN analysis. Yield: 5.7 mg, 31%. IR (KBr, cm^{-1}). CN^- stretching vibrations: 2179m, 2169m, 2152w, 2135w. Anal. Calcd for $Dy_1Mo_1C_{26}\ H_{32}N_{14}O_7$ (M_w = 911.7 g·mol^{-1}): C, 34.28%; H, 3.54%; N, 21.52%. Found: C, 33.90%; H, 3.70%; N, 21.29%.

*$[Ho^{III}(Box)(DMF)_3][Mo^V(CN)_8]{\cdot}MeCN$ (**9**).* The title compound was produced as yellow block crystals. The average size of crystals was much larger than for crystals of **2**–**8** of the similar block shape. The formula was taken from the results of X-ray diffraction experiment. Filtration, washing by Et_2O, and air-drying result in the exchange of solvent molecules of MeCN by H_2O, which gives the air-stable composition of **9**, $[Ho^{III}(Box)(DMF)_3]_2[Mo^V(CN)_8]_2{\cdot}5H_2O$. Yield: 5.0 mg, 27%. IR (KBr, cm^{-1}). CN^- stretching vibrations: 2166sh, 2160sh, 2156m, 2147m, 2120w. Anal. Calcd for $Ho_1Mo_1C_{23}H_{39}N_{13}O_{10}$ (M_w = 918.5 g·mol^{-1}): C, 30.08%; H, 4.28%; N, 19.82%. Found: C, 30.46%; H, 4.50%; N, 19.73%.

*$[Er^{III}(Box)(DMF)_3][Mo^V(CN)_8]{\cdot}MeCN$ (**10**).* The title compound was produced as yellow block crystals. The average size of crystals was much larger than for crystals of **2**–**8** of the similar block shape. The formula was found from the results of X-ray diffraction structural analysis. After filtration, washing by Et_2O, and air-drying, **10** exchanges solvent molecules of MeCN into H_2O to give air-stable composition, $[Er^{III}(Box)(DMF)_3]_2[Mo^V(CN)_8]_2{\cdot}5H_2O$. Yield: 5.1 mg, 28%. IR (KBr, cm^{-1}). CN^- stretching vibrations: 2166sh, 2160sh, 2157m, 2147m, 2120w. Anal. Calcd for $Er_1Mo_1C_{23}\ H_{39}N_{13}O_{10}$ (M_w = 920.8 g·mol^{-1}): C, 30.00%; H, 4.27%; N, 19.77%. Found: C, 29.74%; H, 4.44%; N, 19.48%.

*$[Tm^{III}(Box)(DMF)_3][Mo^V(CN)_8]{\cdot}MeCN$ (**11**).* The title compound was produced as yellow block crystals. The average size of crystals was much larger than for crystals of **2**–**8** of the similar block shape. The formula was found from the X-ray diffraction structural analysis. After filtration, washing by Et_2O, and drying on the air, **11** exchanges solvent molecules of MeCN into H_2O to give air-stable composition, $[Tm^{III}(Box)(DMF)_3]_2[Mo^V(CN)_8]_2{\cdot}5H_2O$. Yield: 4.7 mg, 25%. IR (KBr, cm^{-1}). CN^- stretching vibrations: 2168sh, 2160sh, 2155m, 2147m, 2125w. Anal. Calcd for $Tm_1Mo_1C_{23}\ H_{39}N_{13}O_{10}$ (M_w = 922.5 g·

DOI: 10.1021/acs.inorgchem.5b00040
Inorg. Chem. 2015, 54, 4724–4736

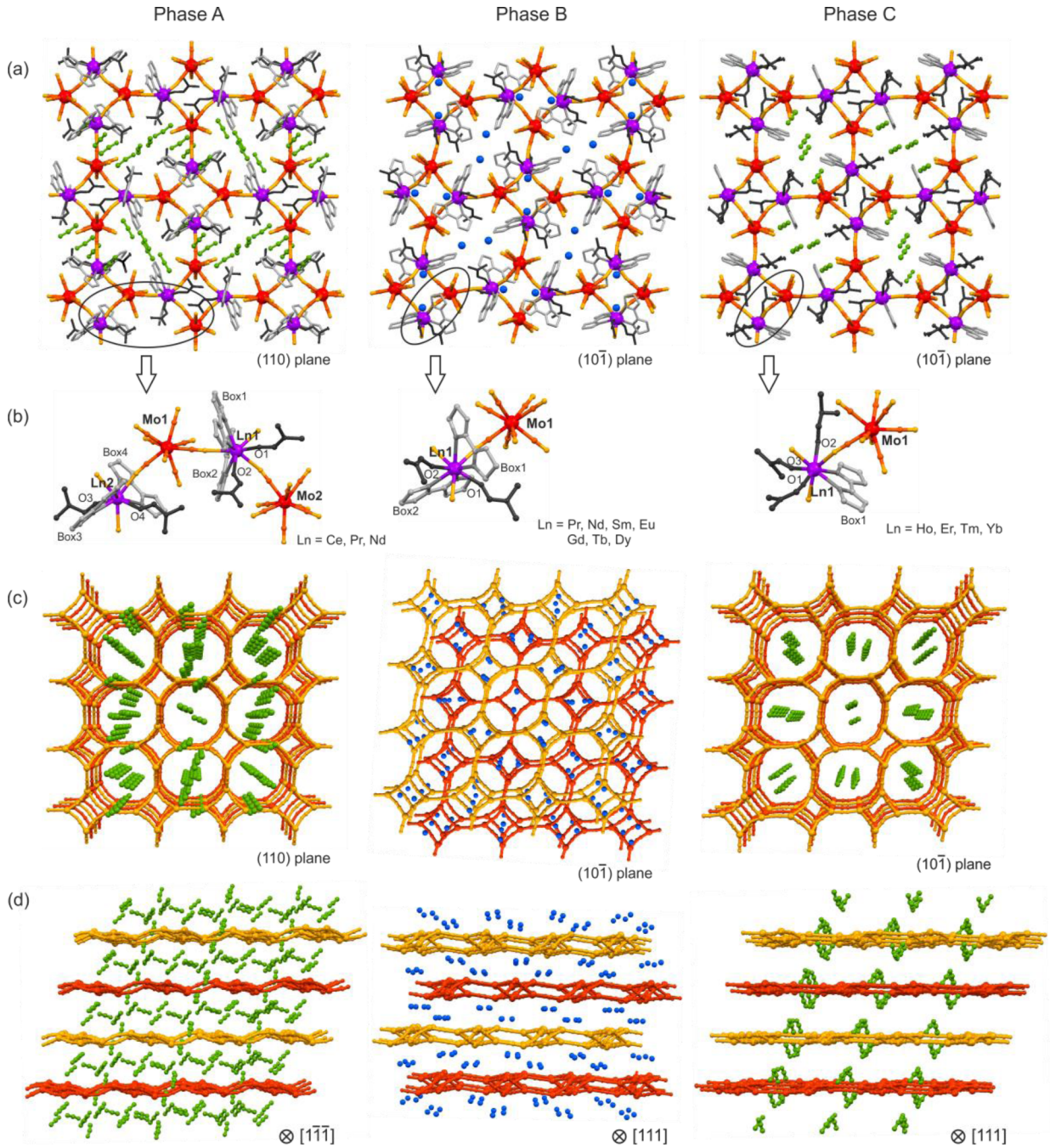

Figure 1. Crystal structures of **1**−**12**: triclinic **type A** phases of **1**, **2a**, and **3a**, monoclinic **type B** phases of **2b**, **3b**, **4**−**8**, and monoclinic **type C** phases of **9**−**12**. Structural views present: (a) the single coordination layer in the perpendicular view, (b) the building unit of coordination layer, and (c, d) the spatial arrangement of layers and solvent molecules between them (acetonitrile−green, water−blue).

mol^{-1}): C, 29.94%; H, 4.26%; N, 19.74%. Found: C, 30.16%; H, 4.32%; N, 20.05%.

*[Yb^{III}(Box)(DMF)$_3$][Mo^{V}(CN)$_8$]·MeCN (**12**).* The title compound was produced as yellow block crystals of the average size of crystals much larger than for crystals of **2**−**8** of the similar shape. The formula was found from the X-ray diffraction structural analysis. Filtration, washing by Et_2O, and air-drying result in the exchange of solvent molecules of MeCN by H_2O, which gives the air-stable composition of **12**, $[Yb^{III}(Box)(DMF)_3]_2[Mo^{V}(CN)_8]_2\cdot 5H_2O$. Yield: 4.0 mg, 22%. IR (KBr, cm^{-1}). CN^- stretching vibrations: 2169sh, 2162sh, 2157m, 2147m, 2126w. Anal. Calcd for $Yb_1Mo_1C_{23}H_{39}N_{13}O_{10}$ (M_w = 926.6 g·mol^{-1}): C, 29.81%; H, 4.24%; N, 19.65%. Found: C, 29.89%; H, 4.38%; N, 19.49%.

Crystal Structure Determination. Single-crystal diffraction data of **1**, **2ab**, **3ab**, and **4**−**12** were collected on a Rigaku R-AXIS RAPID imaging plate area detector with graphite monochromated Mo Kα radiation. The single crystals were dispersed in Apiezon N grease for air-unstable **1**, **2a**, **3a**, **9**−**12**, or Paratone N oil for air-stable **2b**, **3b**, **4**−**8** (Figure S1, Supporting Information). The measurements for **1**−**8** were conducted at 90(2) K and for **9**−**12** at 210(2) or 250(2) K. The crystal structures were solved by a direct method and refined by a full-matrix least-squares technique using SHELXL-97.[49] Calculations were performed using Crystal Structure software and the WinGX

DOI: 10.1021/acs.inorgchem.5b00040
Inorg. Chem. 2015, 54, 4724−4736

(ver. 1.80.05) integrated system. Except for a few disordered solvent molecules in **1**−**3a**, all non-hydrogen atoms in **1**−**12** were refined anisotropically. The hydrogen atoms of **3b**, **4**, **5**, and **7** have been found independently and refined isotropically, whereas the H atoms positions in **1**, **3a**, **9**−**12** have been calculated with an idealized geometry and refined using a riding model. In the cases of **2ab**, **6**, and **8**, the mixed treating of H atoms was applied. Due to the structural disorder, found especially in **1**, **2a**, **3a**, and **9**−**12**, some restraints on C−C and C−N distances in solvent MeCN molecules and weak restraints on thermal ellipsoids of some terminal cyanides, DMF, and solvents have been used in order to maintain the proper geometry. The crystal structures were deposited in CCDC, and the related references numbers are 1039131−1039144 for **1**, **2ab**, **3ab**, **4**−**12**, respectively.

Physical Techniques. IR spectra were recorded on JASCO FTIR-4100 spectrometer in the 4000−400 cm^{-1} range on dried samples mixed with KBr. The UV−vis diffuse reflectance spectra were measured by a Shimadzu UV-3100 spectrometer for dried samples mixed with $BaSO_4$. UV−vis-NIR emission and excitation spectra were collected using a Horiba Jobin-Yvon Fluorolog-3 (FL3-211) spectrofluorimeter (model TKN-7) equipped with a Xe (450 W) lamp as excitation source. For the UV−vis range, a room-temperature R928P emission detector operating in photon-counting mode was applied. For the NIR region, a liquid-nitrogen-cooled version of an InGaAs photodiode detector DSS-IGA020L was used. The emission and excitation data were analyzed using FluorEssence software. To prevent the removal of solvent, all experiments were performed on the crystalline samples covered by a pure solvent. All spectra were collected at 77 K in a cryostat filled with liquid N_2. During long excitation, the emission gradually decreased, probably due to UV-induced photoreactivity involving the photoreduction of $[Mo^V(CN)_8]^{3-}$ moieties and subsequent partial decomposition. This difficulty has been previously observed in other emissive systems built of lanthanides(III) and octacyanidometallates-(V).[20,43] Magnetic properties were investigated using a superconducting quantum interference device (SQUID) magnetometer (Quantum Design). It was confirmed that the magnetic properties of the crystals left in the mother solution and those of the freshly dried samples were identical. Therefore, the results of measurements for only the freshly dried powder samples are presented. The magnetic susceptibility data were corrected for the diamagnetic contributions using Pascal constants.[50]

Calculations. Continuous Shape Measure Analyses for coordination spheres of $[Mo^V(CN)_8]^{3-}$, and Ln^{III} (Ln = Ce−Yb) complexes were performed using SHAPE software ver. 2.1.[51,52]

RESULTS AND DISCUSSION

Crystal Structures. The high-quality single-crystals of **1**−**12** were prepared by layering of Et_2O onto MeCN solutions of $Ln^{III}(NO_3)_3{\cdot}nH_2O$ (Ln = Ce−Yb), Box (bis-oxazoline), and $TBA_3[Mo^V(CN)_8]$ containing a small addition of DMF. Depending on lanthanide(III), three crystalline phases were observed: (i) needles for light lanthanides (Ce, **1**; Pr, **2a**; Nd, **3a**), denoted as **phase A**, (ii) flattened blocks for middle lanthanides (Sm, **4**; Eu. **5**; Gd, **6**; Tb, **7**; Dy, **8**) of **phase B**, found also as a minor phase for Pr (**2b**) and Nd (**3b**), and (iii) larger blocks for heavy lanthanides (Ho, **9**; Er, **10**; Tm, **11**; Yb, **12**), called **phase C** (Figure S1, Supporting Information). Single-crystal X-ray diffraction experiments indicate that phase A is triclinic with *P*-1 space group when phase B and C are monoclinic of *P* $2_1/n$ space group but differing in the unit cell parameters (Table S1−S3). Despite these differences, all compounds, **1**−**12** are cyanido-bridged layers of a mixed 4- and 8-membered metal rings topology (Figure 1, Tables S4−S12 and Figures S2−S6). The layers comprise octametallic $Ln_4Mo_4(CN)_8$ units, built of four $[Mo^V(CN)_8]^{3-}$ ions alternately connected with four Ln^{III} complexes with Box and DMF. The same building blocks create also tetrametallic $Ln_2Mo_2(CN)_4$ squares which link four different $Ln_4Mo_4(CN)_8$ moieties resulting in 2-D coordination skeleton (Figure 1).

Although the overall topology was found to be identical, the details of Ln^{III} coordination sphere and alignment of layers are different for phases A (**1**−**3**), B (**2b**, **3b**, **4**−**8**), and C (**9**−**12**). The asymmetric unit of phase A contains two $[Mo^V(CN)_8]^{3-}$, two $[Ln^{III}(Box)_2(DMF)_2]^{3+}$ ions (Ln = Ce−Nd), and a few disordered MeCN molecules (Figures 1 and S2). Each of the $[Mo^V(CN)_8]^{3-}$ ions form three cyanide bridges, whereas the five remaining cyanides are terminal. Interestingly, Mo1 reveals the geometry of a dodecahedron (DD-8, D_{2d} symmetry), and Mo2 is described as a square antiprism (SAPR-8, D_{4d},Table S8). Ln^{III} coordinates three nitrogen of cyanides, two O atoms of DMF, and four N atoms of two Box ligands, giving a nine-coordinated complex of a capped square antiprism geometry (CSAPR-9, C_{4v}, Table S7). Despite the same coordination spheres, Ln1 and Ln2 differ in the spatial arrangement of ligands. In Ln1, Box ligands are aligned almost parallel with the Box−Box torsion angle close to 160°, when for Ln2, Box rings are perpendicular to each other with the torsion angle ∼90°. Consequently, the O(DMF)−Ln-O(DMF) angle is around 80° for Ln1, while an obtuse angle close to 150° is observed for Ln2.

The asymmetric unit of phase B is constructed of one $[Mo^V(CN)_8]^{3-}$ and one $[Ln^{III}(Box)_2(DMF)_2]^{3+}$ ion accompanied by one H_2O molecule (Figures 1 and S3). Similarly to phase A, the $[Mo^V(CN)_8]^{3-}$ moiety forms three cyanide bridges and reveals a DD-8 geometry (Table S10). The coordination sphere and a CSAPR-9 geometry of Ln1 in phase B is the same as for phase A (Table S9). However, exclusively, one type of spatial arrangement of ligands, with almost perpendicular alignment of Box molecules and Box−Box torsion angle of ∼90°, is observed. In the asymmetric unit of phase C, also only one $[Mo^V(CN)_8]^{3-}$ and one Ln^{III} complex is present, but they are accompanied by one uncoordinated MeCN molecule instead of H_2O, as found in phase B (Figures 1 and S4). The $[Mo^V(CN)_8]^{3-}$ ion forms three cyanide bridges, but the geometry is close to an ideal SAPR-8 (Table S12). Ln^{III} coordinates three N atoms of cyanides, two N atoms of only one Box, and three O atoms of DMF molecules. This gives an eight-coordinated complex of a DD-8 geometry, different to those observed for phases A and B (Table S11). The Ln-dependent variation of crucial structural parameters on going from phase A to B to C was summarized in Figure 2 (see also Tables S4−S6).

The changes in coordination spheres of Ln^{III} in phases A, B, and C affect the size of $Ln_4Mo_4(CN)_8$ and $Ln_2Mo_2(CN)_4$ rings of cyanido-bridged layers. Phase A shows flattened layers with larger rings of 13.7 × 14.0 Å and smaller rings with 5.8 × 5.8 Å size, while multimetallic rings of bent layers in phase B are of the 12.5 × 14.7 Å and 5.8 × 5.8 Å sizes. Phase C reveals almost flat layers with rings of the 13.7 × 13.7 Å and 5.6 × 5.7 Å sizes. The neighboring layers for phases A and C are aligned ideally one above another, so as the large Ln_4Mo_4 rings of one layer are located above the large rings on the next layer, giving the microporous structure built of broad channels with dimensions corresponding to the size of octametallic rings. On the contrary,

DOI: 10.1021/acs.inorgchem.5b00040
Inorg. Chem. 2015, 54, 4724−4736

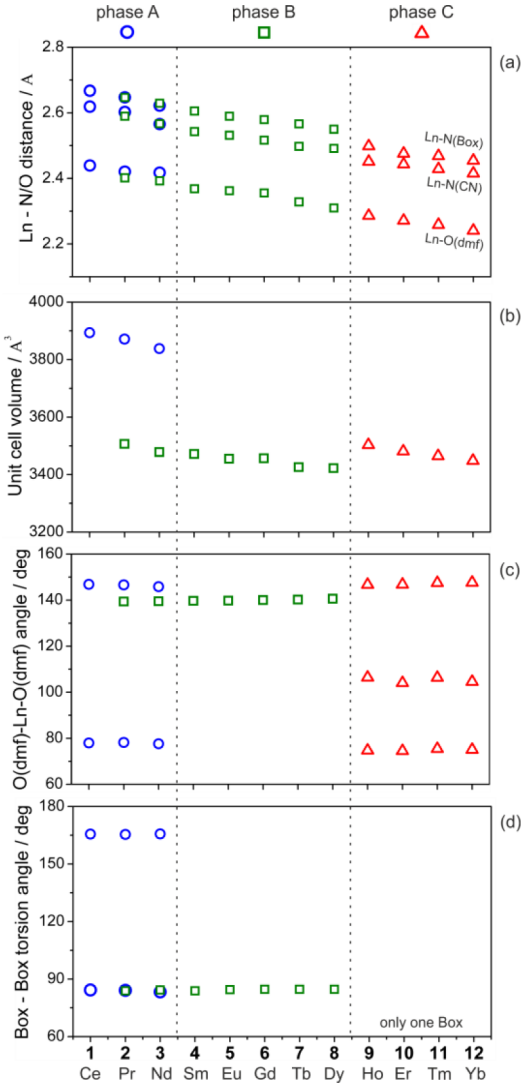

Figure 2. Lanthanide-dependent variation of structural parameters of **1**–**12**: Ln–N/O distances (a), unit cell volume (b), O-Ln-O angle (c), and torsion angle between Box–Box ligands (d).

layers of phase B are arranged with the shift between neighboring layers as the smaller Ln_2Mo_2 squares of one layer are above the larger Ln_4Mo_4 rings of the second (Figure 1). This hampers the size of channels which are the broadest, 8.4 × 10.6 Å, in the [100] or [001] directions, not perpendicular to the plane of CN^--bridged layers (Figure S5). The sliding of coordination layers is accompanied by different solvents in the interlayer space. Between layers of phases A and C, weakly bonded MeCN molecules have been found, while the supramolecular network in phase B is filled by water, stabilizing the interlayer space by strong hydrogen bonds with terminal cyanides. The interactions between layers in phases A and C are dominated by steric effects between DMF and Box, and only weak hydrogen bonds between O atoms of Box and methyl groups of DMF (phase A), or between terminal CN^- and methyl groups of DMF (phase C), are observed (Figure S6).

The two-step sliding of coordination layers on going from phase A to B (step 1) and from phase B to phase C (step 2) depends not only on the nature of lanthanide(III) but also on the change of solvent molecules. Thus, the mechanism involving the correlation between coordination spheres of Ln^{III} and solvent–layer interactions is proposed. Lanthanides(III) reveal a decreasing ionic radius which results in a steady decrease of Ln-N/O bonds (Figure 2). This continuous process induces two-step abrupt changes in Ln^{III} coordination spheres. Large Ce^{III}, Pr^{III}, and Nd^{III} form two types of 9-coordinated $[Ln^{III}(Box)_2(DMF)_2]^{3+}$ units with parallel and perpendicular Box ligands, while Sm^{III} initiates only one type of the complex with parallel Box ligands. Later, Ho^{III} begins the series of 8-coordinated $[Ln^{III}(Box)(DMF)_3]^{3+}$ ions. These different coordination complexes are embedded into the identical cyanido-bridged layers affecting solvent–layer interactions. Due to the synthetic procedure, water molecules, coming only from hydrated Ln^{III} salts, are primarily present in the interlayer space as they have stronger preference to Ln^{III} centers than MeCN. This is connected with the preference of Ln^{III} to oxygen coordination and with the stabilization of water by hydrogen bonds with terminal cyanides. We found that terminal cyanides are open for hydrogen bonds with solvent only for phase B, while for phase A and C, they are protected by hydrophobic hydrocarbon groups of DMF and box. As a result, the hydrogen bonding network is only formed for phase B, and we observe the related sliding of coordination layers. In phases A and C, where MeCN molecules are present, the steric effects dominate, and the microporous network with large channels is induced (Figure S7).

Optical Properties. Except for compound **1**, which reveals a green color, the crystals of all other compounds are yellow, which is related to the ligand-to-metal charge transfer (LMCT) of $[Mo^V(CN)_8]^{3-}$ ions giving the strong absorption from the UV to blue-violet range (Figure S1 and S8).[46,53] In a special case of **1**, the additional absorption around 620 nm can be assigned to Ce^{III}–Mo^V metal-to-metal charge transfer (MMCT) as the Ce^{IV} and Mo^{IV} oxidation states are optically accessible.[54,55] Taking advantage of strong absorption in the UV range, the luminescence properties of **1**–**12** were investigated by means of solid-state emission and excitation spectra at liquid nitrogen temperature, and the results are presented in Figures 3–5 and S9–S11.

Under irradiation of UV light, **2**, **4**, **5**, and **9** exhibit the visible luminescence consisting of sharp peaks of f–f transitions (Figure 3). **2** reveals red emission coming from three peaks at 625, 725, and 798 nm (Figure 3). This is ascribed to phosphorescent f–f transitions from $^1D_2$ state of Pr^{III} to ^3H_J (J = 4, 5, 6) multiplets. Sm^{III}-based **4** shows an orange color of emission due to the peak at 595 nm, accompanied by weaker bands at 560, 645, 708, and 790 nm. They are related to f–f $^4G_{5/2} \rightarrow {}^6H_J$ (J = 5/2, 7/2, 9/2, 11/2, 13/2) transitions. The red phosphorescence is observed also for **5** due to Eu^{III}-centered $^5D_0 \rightarrow {}^7F_J$ (J = 0, 1, 2, 3, 4, 5, 6) transitions giving the maxima at 580, 592, 615, 650, 695, 750, 810 nm, respectively. The different, yellowish green emission was detected for Ho^{III}-based **9**, which is caused by the dominant peak at 545 nm assigned to $^5S_2 + {}^5F_4 \rightarrow {}^5I_8$ fluorescence. Other transitions from $^5S_2 + {}^5F_4$ state to the $^5I_7$ multiplet and from different $^5F_5$ emissive state to the $^5I_8$ ground state gave weaker peaks at 655 and 760 nm, respectively. In the excitation spectra of **2**, **4**, **5**, and **9**, a broad band centered around 350 is observed, suggesting the energy transfer process from Box coordinated to Ln^{III}. This is supported by the absence of Box emission, which is expected to be ~480 nm, and ~640 nm, respectively.[20] Besides the energy transfer mechanism, the direct intra-f excitation is possible in all compounds, as manifested by a series of sharp peaks in the excitation spectra. The other possible energy transfer pathway applying absorption to high energy ligand-to-metal charge transfer (LMCT) O → Eu band was detected for Eu^{III}-

DOI: 10.1021/acs.inorgchem.5b00040
Inorg. Chem. 2015, 54, 4724–4736

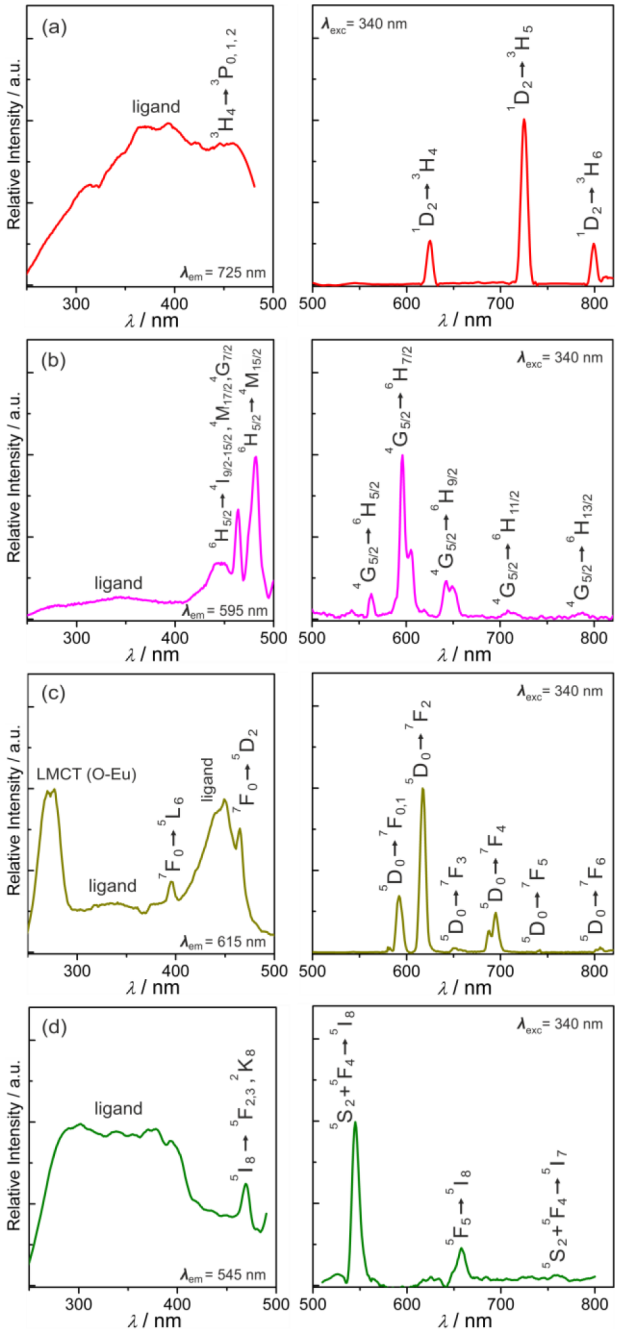

Figure 3. Solid-state visible emission (right) and excitation (left) spectra at T = 77 K for **2** (a), **4** (b), **5** (c), and **9** (d) revealing ligand-to-metal energy transfer.

based **5**.[21] Because of the sample preparation and the nature of solid state measurements, it is difficult to compare the luminescence intensity of **2**, **4**, **5**, and **9** and the related efficiency of energy transfer. However, a rough comparison showed that Eu^{III} in **5** reveals the emission ~10 times stronger than observed for other Ln^{III} in **2**, **4**, and **9** (Figure S9).

The visible emission was also found for **6** and **7** (Figure 4). Due to the presence of Gd^{III}, **6** cannot reveal f-centered emission, but it allows the observation of the broad red $^3T_1 \rightarrow {}^1S_0$ phosphorescence of Box at 630 nm.[20] Using 340 nm excitation light, a similar broad band ascribed to the $^3T_1 \rightarrow {}^1S_0$ transition in Box was found for Tb^{III}-containing **7**. However, by using the higher energy excitation of 270 nm, the green emission

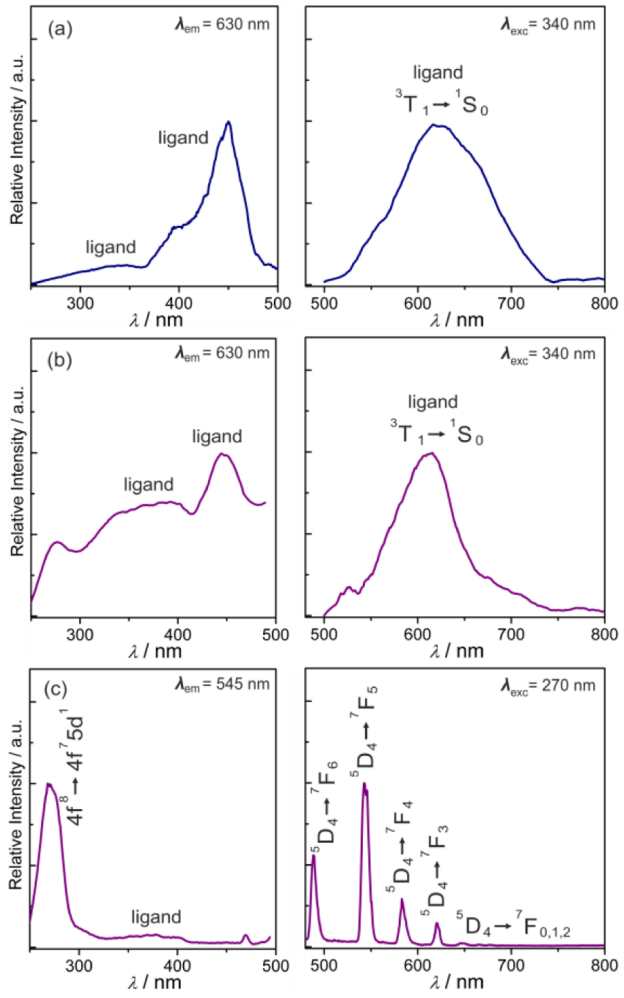

Figure 4. Solid-state visible emission and excitation spectra at T = 77 K for **6** (a) and **7** under the excitation by light of 340 (b) and 270 nm (c).

represented by sharp peaks at 490, 545, 583, and 620 nm is observed. This can be assigned to characteristic f–f $^5D_4 \rightarrow {}^7F_J$ (J = 6, 5, 4, 3) transitions in Tb^{III}. The different color of emission originates from the selective excitation of ligand and Ln^{III} states as visible in the excitation spectra.[20] For ligand emission, the expected broad band with the maxima at 360 and 440 nm is observed, when for Tb^{III} emission, the strong peak is present at high energy of 260 nm, which is ascribed to the $4f^8 \rightarrow 4f^7 5d^1$ transition.[56,57] The direct Tb^{III} excitation is more efficient than the phosphorescence of organic ligand, as found by a rough comparison of experimental intensities (Figure S10).

Using the irradiation of Box ligand with 340 nm line, **2**, **3**, **4**, **9**, and **12** emit the light in NIR range (Figure 5). **2** shows dominant peak built of two components at 990 and 1020 nm, accompanied by weaker emission at 865 nm. They can be assigned to the f–f transitions from the $^1D_2$ state to ^3F_J (J = 2, 3, 4) multiplets (Figure 5). The NIR Nd^{III}-centered fluorescence was found for **3**, revealing sharp peaks at 900 and 1060 nm due to the $^4F_{3/2} \rightarrow {}^4I_J$ (J = 9/2, 11/2) transitions. The emission in the similar region was found for Sm^{III} in **4**, where the maxima at 895, 940, and 1060 nm are detected. They are related to a complicated series of phosphorescent transitions from the $^4G_{5/2}$ to $^6H_{15/2}$ and various ^6F_J (J = 1/2, 3/2, 5/2, 7/2) states. The broader NIR emission was found for **9**, exhibiting a complex band with two components at 980 and 1060 nm, explained by $^5F_5 \rightarrow {}^5I_7$ and $^5S_2 + {}^5F_4 \rightarrow {}^5I_6$

DOI: 10.1021/acs.inorgchem.5b00040
Inorg. Chem. 2015, 54, 4724–4736

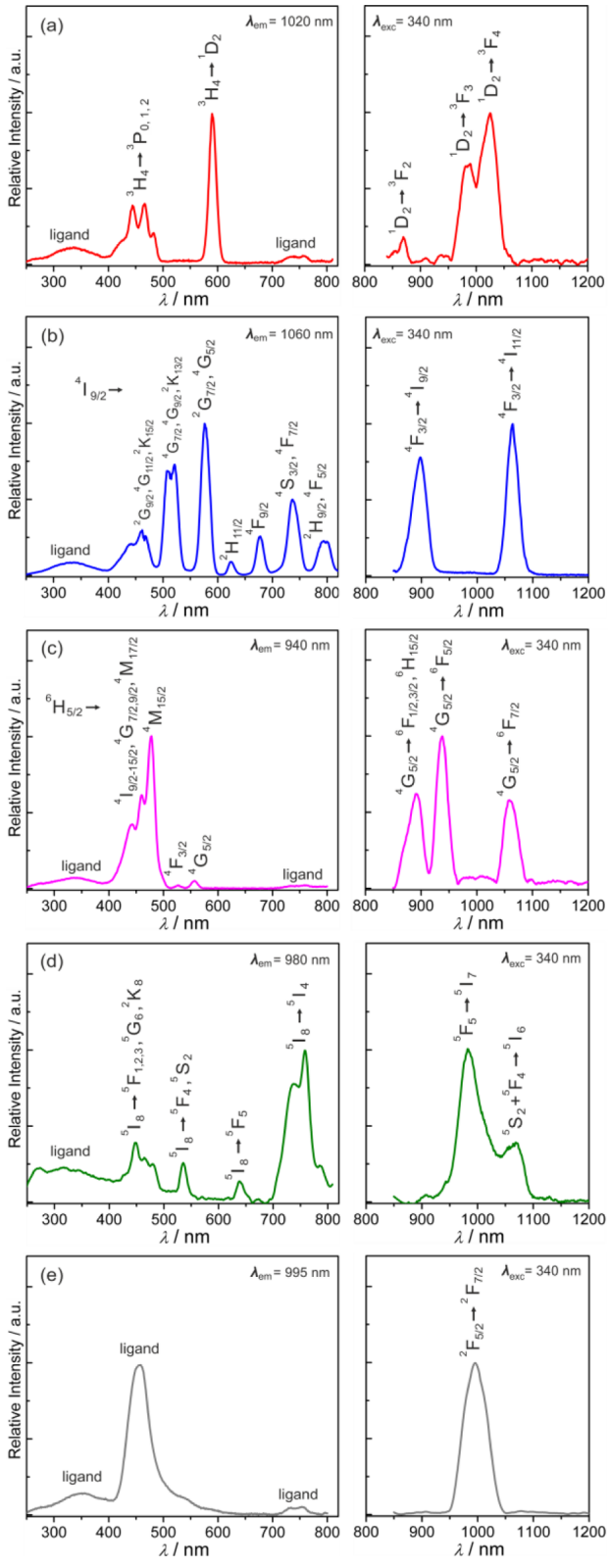

Figure 5. Solid-state near-infrared emission spectra at T = 77 K (right) and the related excitation spectra in the UV–vis range (left) for **2** (a), **3** (b), **4** (c), **9** (d), and **12** (e).

fluorescent transitions, respectively. The emitted NIR light was observed also for **12**, which reveals characteristic single peak at 995 nm of an Yb^{III}-centered $^2F_{5/2} \rightarrow {}^2F_{7/2}$ origin. This compound is specific as Yb^{III} has no other f–f states, and the excitation spectrum contains only the ligand-based bands at 350 and 455 nm, indicating the ligand-to-metal energy transfer mechanism in **12**. The similarly located maxima of excitation were found for all NIR-emitting **2**, **3**, **4**, and **9**, but they exhibit also the direct-f excitation pathways by various wavelengths of visible light. In the rough comparison of the experimental intensities of NIR emission, the strongest peaks are those for Nd^{III} of **3**, which are four times stronger than for Yb^{III} in **12** and more than 20 times stronger than peaks from other Ln^{III} in **2**, **4**, and **9** (Figure S11).[58]

The complementary studies of UV–vis-NIR absorption, emission, and excitation spectra allow us to construct the energy level diagram showing all luminescent effects, and accompanying processes of **1**–**12** (Figure 6). The observed optical phenomena depends on the relative position between the triplet state of Box and the emissive state of Ln^{III}. In **2**, **3**, **4**, **5**, **9**, and **12**, at least one emissive state of Ln^{III} is within or below the range of Box $^3T_1$ energy level, and thus, the energy transfer (ET) from Box to Ln^{III} can be observed. For **2**, Pr^{III} has two possible emissive levels, but $^3P_0$ is located too high for Box donors, and the emission from only $^1D_2$ can be detected. In NIR-emitting **3** and **12**, the Nd^{III} and Yb^{III} emissive states are situated below the $^3T_1$ state, and ET is preferred. The emissive states of Sm^{III} and Eu^{III} are located in similar positions, both reasonably good for ET, which results in vis–NIR, or only vis emission, respectively. Ho^{III} is a special case, possessing three too closely positioned emissive states, and all of them are within the range accessible for ET, so the complex vis–NIR luminescent characteristics are observed in **9**. The potentially emissive states of Gd^{III}, Tb^{III}, Dy^{III}, and Tm^{III}, are situated too high for ET from Box. For Gd^{III}-based **6** and Tb^{III}-based **7**, it results in ligand phosphorescence because the energy is not lost, as no other energy levels overlap with the $^3T_1$ state of Box. It gave also the selective excitation of Tb^{III} by using higher energy light. There is lack of even Box emission in **8** and **11**, which is due to overlap between nonemissive states of Dy^{III} and Tm^{III}, with Box, inducing the nonradiative relaxation. The ET giving the emission could be also found for Er^{III}-containing **10**; however, there is no signal, which is due to relaxation through the vibration modes, crucial for a small gap Er^{III} NIR emitters.[58] The lack of emission in **1** is due to the overlap between $^3T_1$ state of Box, and Ce^{III}–Mo^{V} MMCT band of **1**, and energy can be transferred from Box, but MMCT levels involving $[M^{V}(CN)_8]^{3-}$ are not emissive. There is no contribution from $[Mo^{V}(CN)_8]^{3-}$ ions to the emission, which means that energy absorbed by their LMCT states are relaxed, not influencing on the equilibrium between Ln^{III} and Box.

Magnetic Properties. Compounds **1**–**12** consist of two paramagnetic centers, Mo^{V} and Ln^{III}, which can be magnetically coupled through cyanide bridges.[42] The significant magnetic couplings were found for **1**, **3**, **4**, **6**–**8**, and their properties are presented below (Figures 7–11), while the magnetism of **2**, **5**, **9**–**12**, is dominated by standard single-ion properties of the respective lanthanide(III) ion, so as they are discussed only in the Supporting Information (Figures S12–S14).

Compound **1**. The room-temperature $\chi_M T$ is 1.04 $cm^3\ mol^{-1}$ K for $\{Ce^{III}Mo^{V}\}$ unit in agreement with the expected 1.18 $cm^3\ mol^{-1}$ K for the uncoupled pair of Ce^{III} (J = 5/2, g_J = 6/7) and Mo^{V} (S = 1/2, g = 2).[59] On cooling, the $\chi_M T$ gradually decreases to 0.86 $cm^3\ mol^{-1}$ K at 12 K, which is followed by abrupt increase to 0.99 $cm^3\ mol^{-1}$ K at 1.8 K (Figure 7). The steady decrease of the $\chi_M T$ is ascribed to the thermal depopulation of the Stark levels arising from the splitting of the $^2F_{5/2}$ ground state of Ce^{III}, whereas the further increase can be assigned to magnetic

DOI: 10.1021/acs.inorgchem.5b00040
Inorg. Chem. 2015, 54, 4724–4736

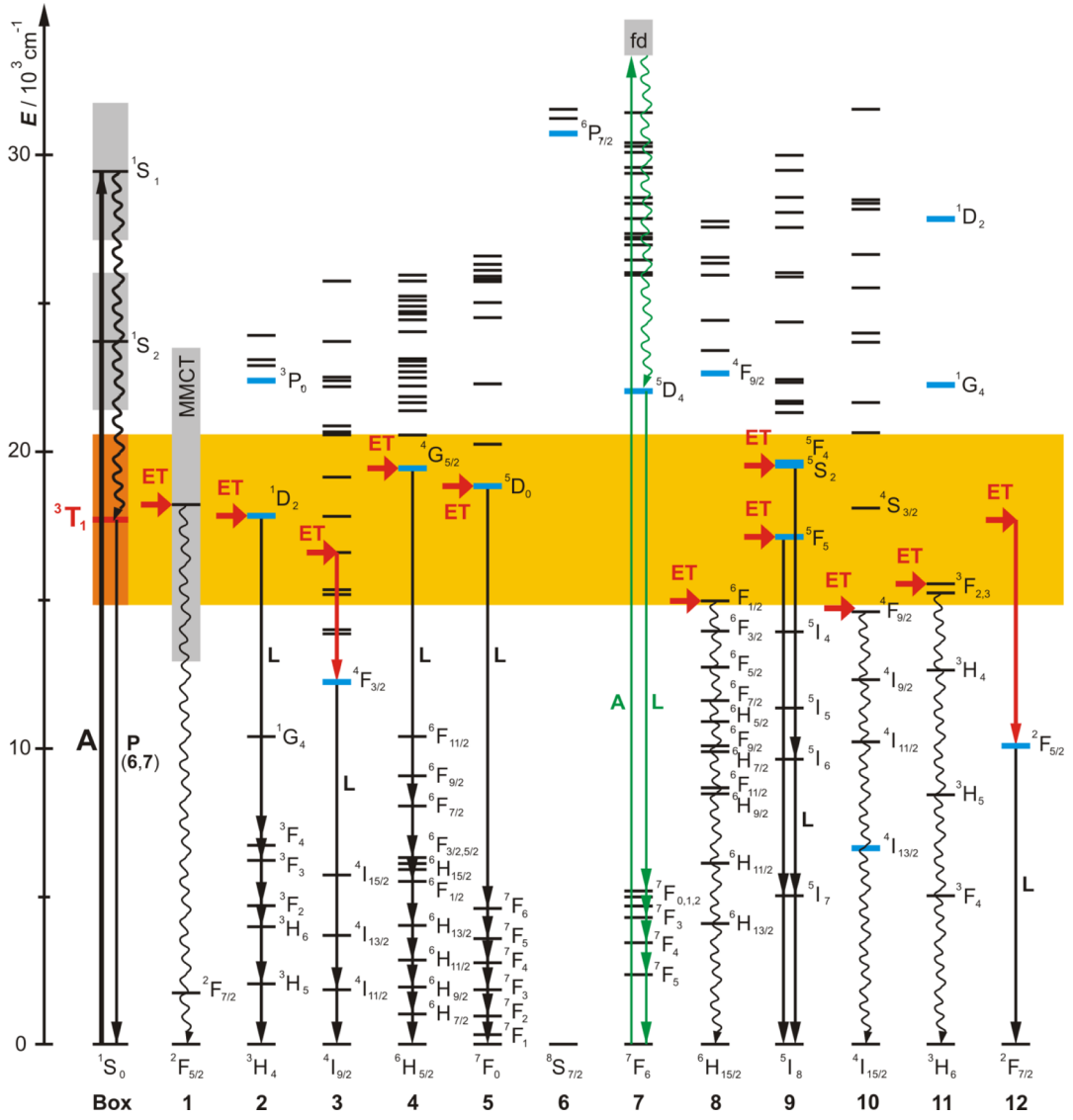

Figure 6. Schematic energy level diagram explaining the mechanism of luminescent effects in **1**–**12**. The straight lines correspond to absorption or emission, while the wavy lines present nonradiative relaxation. The ligand-to-metal energy transfer (ET) is presented as red arrows. The range of $^3T_1$ ligand state was shown as the orange background, when the emissive states are presented as thick blue lines. The processes occurring under the irradiation by 340 nm wavelength were presented by black and red arrows, while the separate mechanism of direct excitation of Tb^{III} using the light of 270 nm was shown using green arrows. Abbreviations: A – absorption, P – ligand phosphorescence, L – lanthanide luminescence, ET – energy transfer.

interactions within Ce^{III}–NC–Mo^V linkages.[60] The magnetization at T = 1.8 K increases with increasing magnetic field to 1.83 Nβ at 50 kOe, which is close to the range of 1.85–2.07 Nβ expected for combined contributions from Ce^{III} and Mo^V, assuming a spin of S = 1/2 with g = 2 for Mo^V, and an effective spin of S_{eff} = 1/2 with g within the range of 1.71–2.15 for Ce^{III}.[60] The M at 50 kOe in **1** is higher than 1.61 Nβ found for one example of Ce^{III}–Mo^V system for which positive J value of 1.4 cm^{-1} was proved.[61] All these suggest a ferromagnetic type of Ce^{III}–Mo^V coupling in **1**. However, these interactions are weak, and FCM curves do not show abrupt increase of the signal, and ac signal is negligible (not shown), indicating the lack of magnetic ordering.

Compound ***3***. At room temperature, the $\chi_M T$ reaches 1.67 $cm^3\ mol^{-1}$ K for {$Nd^{III}Mo^V$}, which is lower than the value of 2.01 $cm^3\ mol^{-1}$ K expected for the isolated pair of Nd^{III} (J = 9/2, g_J = 8/11) and Mo^V (S = 1/2, g = 2). This is connected with thermal depopulation of Nd^{III} Stark levels of the $^4I_{9/2}$ ground state, which are not equally populated even at 300 K. This implies further decrease of $\chi_M T$ with decreasing temperature up to 1.07 $cm^3\ mol^{-1}$ K at 9 K (Figure 7). On the contrary, the abrupt increase of $\chi_M T$ below 9 K up to 1.43 $cm^3\ mol^{-1}$ K at 1.8 K has to be connected with the Nd^{III}–Mo^V magnetic coupling. The magnetization at T = 1.8 K increases fast with increasing field giving the value of 2.13 Nβ, close to 2.25 Nβ calculated for a parallel alignment of Mo^V (S = 2, g = 1/2) and Nd^{III} (S_{eff} = 1/2, g_{eff} = 2.5) magnetic moments. This together with the shape of $\chi_M T$–T curve suggest the ferromagnetic character of Nd^{III}–Mo^V interactions, which agrees well with other reports on octacyanido-based compounds with Nd^{III}.[42,44,46] As validated by FCM curves showing only slow increase of the signal and ac measurements revealing no detectable signal (not shown), these interactions are too weak to induce magnetic ordering in **3**.

Compound ***4***. Upon cooling, the $\chi_M T$–T curve reveals almost linear decrease from the value of 0.82 $cm^3\ mol^{-1}$ K for {$Sm^{III}Mo^V$} unit at 300 K to 0.50 $cm^3\ mol^{-1}$ K at 13 K (Figure 8). The

DOI: 10.1021/acs.inorgchem.5b00040
Inorg. Chem. 2015, 54, 4724–4736

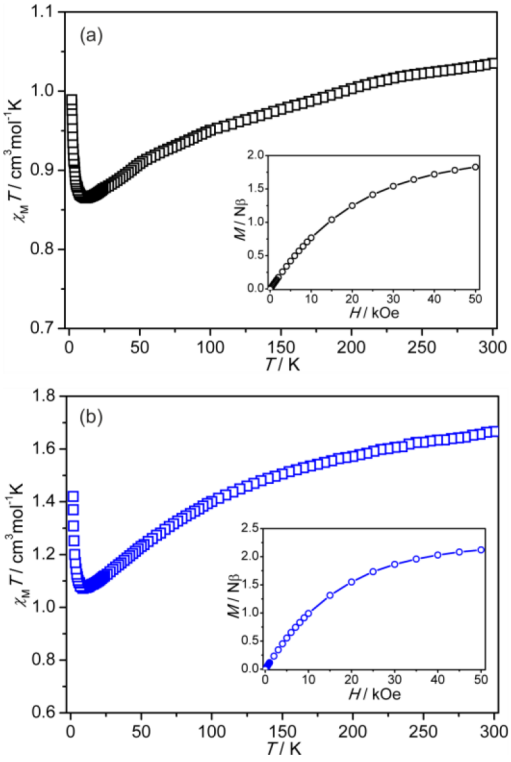

Figure 7. Magnetic properties of **1** (a) and **3** (b): $\chi_M T$ versus T plots at H = 2 kOe, and M versus H curves at T = 1.8 K in the insets.

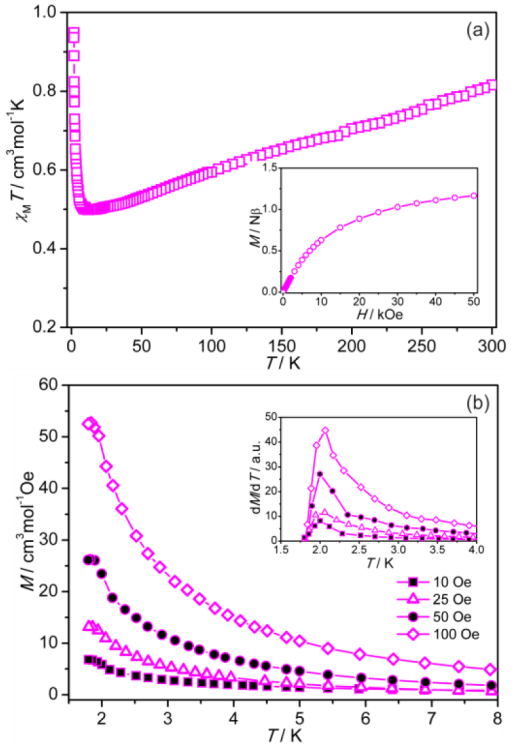

Figure 8. Magnetic properties of **4**: $\chi_M T$–T plot (H = 2 kOe) (a), H dependence of M at T = 1.8 K (a, the inset), and FCM curves at various H with its first derivative in the inset (b).

room-temperature $\chi_M T$ is higher than 0.46 cm^3 mol^{-1} K expected for the isolated Sm^{III} (J = 5/2, g_J = 2/7) and Mo^V (S = 1/2, g = 2).[59] These characteristics are related to the special properties of Sm^{III} for which not only Stark multiplets of the $^6H_{5/2}$ ground state but also the low-lying $^6H_{7/2}$ excited state can be populated at high temperature. At low temperatures, the abrupt increase of the $\chi_M T$ product up to 0.95 cm^3 mol^{-1} K at 1.8 K is observed, and this can be ascribed to the Sm^{III}–Mo^V interactions. They are relatively strong as the fast increase of magnetization in the M–H plot is observed. The value of M at 50 kOe is equal 1.22 Nβ, which is close to 1.28 Nβ expected for ferromagnetically coupled Sm^{III}–Mo^V pair, assuming a spin of S = 1/2 with g = 2 for Mo^V and an effective spin of S_{eff} = 1/2 with the average g value of 0.57 for Sm^{III}.[63] At the same time, it is much higher than 0.72 Nβ calculated for the antiferromagnetic alignment of Sm^{III} and Mo^V magnetic moments. This indicates a ferromagnetic character of coupling, similar to other Sm^{III}–[M^V(CN)$_8$]$^{3-}$ systems.[21,42,62] Moreover, FCM curves show the abrupt increase at low temperatures and further saturation, indicating a ferromagnetic ordering in **4**. The critical temperature of T_c = 2.0 K was estimated from the first derivative of FCM. The onset of magnetic ordering was confirmed by ac magnetism, however, the peak in $\chi''_M T(T)$ plot was not clearly formed due to low T_c (Figure S12).

Compound **6**. The $\chi_M T$ product for {Gd^{III} Mo^V} unit at 300 K reaches 8.26 cm^3 mol^{-1} K, which agrees well with the isolated pair of Gd^{III} (S = 7/2, g = 2) and Mo^V (S = 1/2, g = 2). On cooling, the $\chi_M T$ is stable up to 100 K and later decreases to 7.81 cm^3 mol^{-1} K at 11 K, which is followed by the abrupt increase to a maximum of 15.2 cm^3 mol^{-1} K at 2 K (Figure 9). As Gd^{III} has no first-order

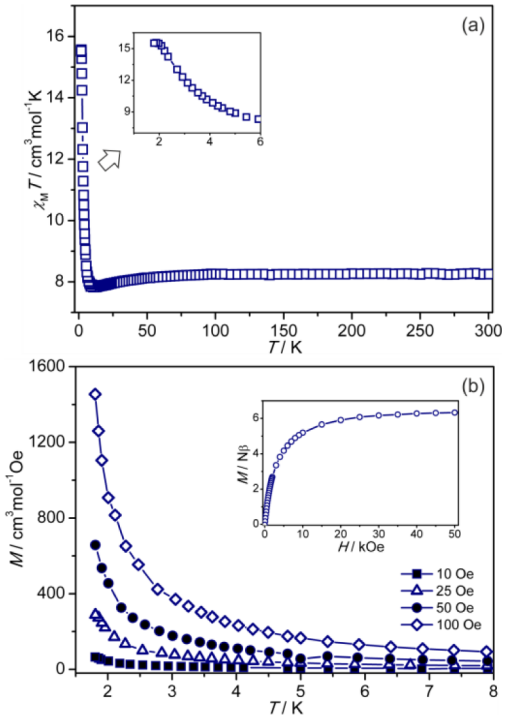

Figure 9. Magnetic properties of **6**: T dependence of $\chi_M T$ (H = 2 kOe) (a), FCM curves at various H (b), and H dependence of M at T = 1.8 K (b, the inset).

orbital contribution, the minimum on $\chi_M T$–T plot indicates the Gd^{III}–Mo^V antiferromagnetic coupling, which is later spread within the layers giving the large increase of $\chi_M T$. This interpretation is supported by the M–H curve showing a fast increase to 6.2 Nβ at 50 kOe, close to 6.0 Nβ expected for the antiferromagnetically coupled Gd^{III}–Mo^V pair. The maximum on $\chi_M T$–T plot at low temperatures can suggest the transition to

DOI: 10.1021/acs.inorgchem.5b00040
Inorg. Chem. 2015, 54, 4724–4736

the ordered state. In fact, FCM curves show a fast increase of signal at low T, but the saturation is not reached, indicating that T_c is on the border of the measurement range, which is also observed in ac magnetism (Figure S12).

Compound **7**. At room temperature, the $\chi_M T$ value of $\{Tb^{III}Mo^{V}\}$ unit is 12.2 $cm^3\ mol^{-1}\ K$, which is the same as calculated for the uncoupled Tb^{III} ($J = 6, g_J = 3/2$)$-Mo^{V}$ ($S = 1/2, g = 2$) pair.[59] Upon cooling, $\chi_M T$ is stable to 100 K and later decreases to minimum of 11.2 $cm^3\ mol^{-1}\ K$ at 11 K, which is followed by the increase to 19.5 $cm^3\ mol^{-1}\ K$ at 2.5 K. At the lowest T, a further decrease of $\chi_M T$ is observed (Figure 10). The minimum on the

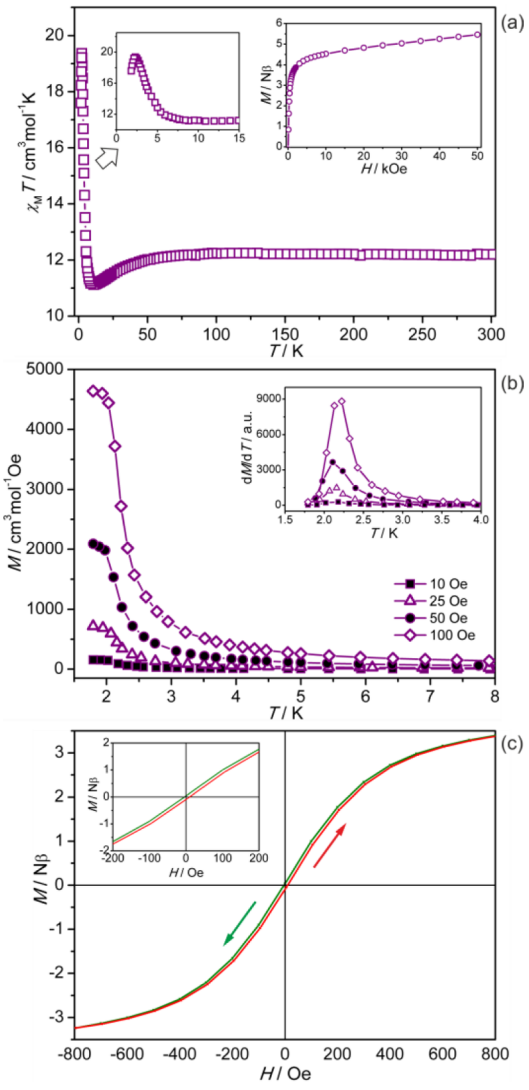

Figure 10. Magnetic properties of **7**: $\chi_M T-T$ plot ($H = 2$ kOe) (a), $M-H$ curve at $T = 1.8$ K (a, the inset), FCM curves at various H with its first derivative in the inset (b), and $M-H$ hysteresis loop at $T = 1.8$ K (c).

$\chi_M T-T$ curve is related to the thermal depopulation within the multiplets of $^7F_6$ ground state of Tb^{III}, whereas the increase below 11 K is due to $Tb^{III}-Mo^{V}$ magnetic coupling.[60] Its character is suggested by the $M-H$ plot showing the value of 5.6 Nβ at 50 kOe without saturation, which is close to 6.0 Nβ calculated for the ferromagnetically coupled Tb^{III} ($S_{eff} = 1/2, g_{eff} = 10$)$-Mo^{V}$ ($S = 1/2, g = 1/2$) unit. The very low T maximum on $\chi_M T(T)$ plot suggests the onset of magnetic ordering, which is easily visible in the FCM curves revealing an abrupt increase below 2.5 K, followed by saturation of M. The T_c value of 2.2 K was determined by the first derivative of FCM. Compound **7** reveals narrow magnetic hysteresis with small coercive field of 12 Oe. The ac magnetic signals reveal also peaks typical for the magnetic phase transition. However, there is a weak frequency dependence, suggesting the contribution of spin glass behavior coexisting with ferromagnetism in **7**.[20,63] The similar dependences, but at lower temperatures, were observed also in **4** and **6**, supporting the interpretation of a 3-D spin glass effect rather than the role of magnetic anisotropy (Figure S12).

Compound **8**. The $\chi_M T$ for $\{Dy^{III}Mo^{V}\}$ unit reaches at 300 K the high value of 14.4 $cm^3\ mol^{-1}\ K$, close to the expected 14.5 $cm^3\ mol^{-1}\ K$ for the isolated Dy^{III} ($J = 15/2, g_J = 4/3$)$-Mo^{V}$ ($S = 1/2, g = 2$) pair.[59] On cooling, the $\chi_M T-T$ plot is flat, while the gradual decrease is detected below 50 K, with the minimum of 12.7 $cm^3\ mol^{-1}\ K$ at 9 K, which can be assigned to the depopulation of numerous multiplets within Dy^{III} $^6H_{15/2}$ ground state (Figure 11). On further cooling, the rapid increase of signal

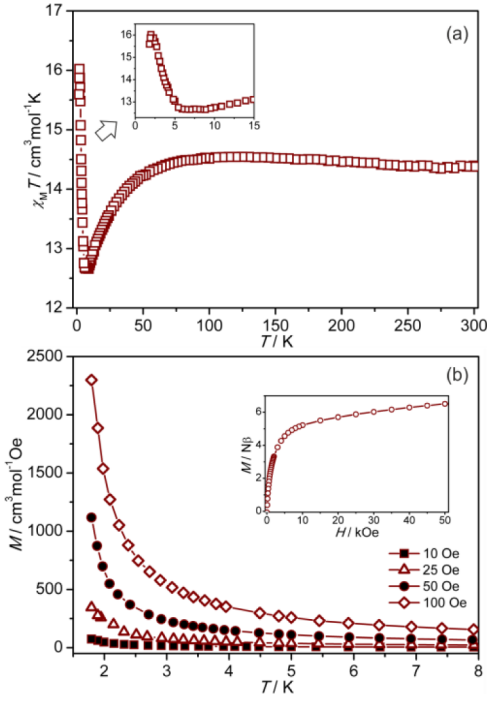

Figure 11. Magnetism of **8**: $\chi_M T-T$ plot ($H = 2$ kOe) (a), FCM curves (b), and $M-H$ curve at $T = 1.8$ K (b, the inset).

is observed, and after the maximum at 2.2 K, the $\chi_M T$ finally decreases. These features relate to magnetic interactions within $Dy^{III}-NC-Mo^{V}$. The $M-H$ plot shows fast increase of magnetization to the value of 6.6 Nβ at 50 kOe without saturation. This high value can suggest the ferromagnetic type of $Dy^{III}-Mo^{V}$ coupling, consistent with the previous report,[42] but the contribution from Dy^{III} to the M strongly depends on detailed distribution of its Stark levels.[61] Taking the average value of $g_{Dy} = 9.3$ from simple inorganic salts, the prediction for ferromagnetic Dy^{III} ($S_{eff} = 1/2$)$-Mo^{V}$ pair is 5.7 Nβ, while for antiferromagnetic case only 3.7 Nβ, suggesting the ferromagnetic interactions in **8**. The maximum on $\chi_M T-T$ plot at very low T indicate the transition to the ordered state. FCM curves show fast increase of signal at low T, but the saturation is not reached up to 1.8 K, indicating that T_c is at the limit of the measurement range, which is also observed in ac magnetism (Figure S12).

DOI: 10.1021/acs.inorgchem.5b00040
Inorg. Chem. 2015, 54, 4724−4736

CONCLUSIONS

We have prepared and studied in detail a series of 4f−4d cyanido-bridged coordination polymers, $\{[Ln^{III}(Box)_n(DMF)_m][Mo^{V}(CN)_8]\}\cdot x(solvent)$ (**1**−**12**) of a bifunctional magneto-luminescent character. We found the unusual two-step sliding of their coordination layers on going from $\{[Ln^{III}(Box)_2(DMF)_2][Mo^{V}(CN)_8]\}\cdot 1.5MeCN$ phase A of light Ce−Nd, through intermediate $\{[Ln^{III}(Box)_2(DMF)_2][Mo^{V}(CN)_8]\}\cdot H_2O$ phase B (Sm−Dy) to $\{[Ln^{III}(Box)(DMF)_3][Mo^{V}(CN)_8]\cdot MeCN$ phase C of heavy lanthanides, (Ho−Yb).

Although light and heavy lanthanides show similar microporous structures with large channels due to the ideal "one above another" arrangement of the layers, intermediate lanthanides reveal shifted positions of layers giving much smaller pores. We explained this by the changes in the coordination sphere of Ln^{III} influencing the solvent−layer interactions. Although the solvent-dependent sliding of coordination layers was previously shown,[64] we have shown for the first time how such lanthanides exert control over the preference of solvent and the related sliding of layers.

We have also proved that $[M(CN)_8]$-based coordination polymers with embedded 4f metal ions coordinating the additional emissive organic molecule can be convenient molecular platforms to induce a diversity of luminescent effects. We have shown the ligand-to-metal energy transfer resulting in the multicolored Ho^{III} green, Sm^{III} orange, and Pr^{III} or Eu^{III} red f-centered emission or in the near-infrared luminescence of five different characteristics found for Pr^{III}, Nd^{III}, Sm^{III}, Ho^{III}, and Yb^{III}-based materials. We presented ligand emission in Gd^{III} containers and selective excitation of ligand or metal excited states giving red to green emission in Tb^{III}−Mo^{V}. *Thus, we expanded a set of cyanido-bridged bimetallic luminophors, showing for the first time Pr^{III}, Sm^{III}, and Ho^{III} emission in the cyanido-bridged assemblies.*

Taking advantage of paramagnetism in both types of 4f and 4d metal ions connected by cyanide bridges in **1**−**12**, we showed the magnetic coupling, and magnetic ordering observed in the Sm^{III}−Mo^{V} (T_c = 2.0 K), Tb^{III}−Mo^{V} (T_c = 2.2 K), Gd^{III}−Mo^{V} ($T_c \sim$ 1.8 K), and Dy^{III}−Mo^{V} ($T_c \sim$ 1.8 K) analogues. Thus, we can consider the obtained coordination polymers as a rare family of magneto-luminescent molecular materials. In this aspect, the organic ligand controls the topology of **1**−**12**, giving the possibility to observe magnetic coupling within the cyanido-bridged network. The presented discussion on mechanisms govern the structural dynamics, optical and magnetic properties which can be used in the improvement of magneto-luminescent bifunctionality of **1**−**12**, and similar materials. Modification of synthetic conditions should give the control over the sliding of coordination of layers and the resulting microporous structures which can be explored as a potential source of magneto-luminescent sensing. The introduction of modified ligand can amend the optical properties and the magnetism through changes in a cyanido-bridged connectivity. The insertion of chiral species is another interesting route, and enantiopure bis(oxazoline) ligands can be achievable. These enhancements will expand the multifunctional potential of the materials. These perspectives are worth investigating in the near future.

ASSOCIATED CONTENT

Supporting Information

Photos of crystals, crystal data, results of analyses of coordination polyhedrons, structural views, description of UV−vis absorption spectra, comparison of emission intensities, analysis of ac magnetism, and magnetic properties of **2**, **5**, **9**−**12**. The Supporting Information is available free of charge on the ACS Publications website at DOI: 10.1021/acs.inorgchem.5b00040.

AUTHOR INFORMATION

Corresponding Authors

*E-mail: ohkoshi@chem.s.u-tokyo.ac.jp.

*E-mail: barbara.sieklucka@uj.edu.pl.

Author Contributions

The manuscript was written through contributions of all authors. All authors have given approval to the final version of the manuscript.

Notes

The authors declare no competing financial interest.

ACKNOWLEDGMENTS

The research was supported by the Core Research for Evolutional Science and Technology (CREST) program of the Japan Science and Technology Agency (JST), Advanced Photon Science Alliance (APSA) from the Ministry of Education, Culture, Sports, Science and Technology of Japan (MEXT), Global Science course from MEXT, the Cryogenic Research Center, The University of Tokyo, the Center for Nano Lithography and Analysis, The University of Tokyo, supported by MEXT, Grant-in-Aid for Specially Promoted Research of JSPS (JSPS Kakenhi grant number 15H05697), and by the Polish National Science Centre − Research Project DEC-2011/01/B/ST5/00716. S.C. acknowledges the financial support of the Foundation for Polish Science within the START fellowship (edition 2014).

REFERENCES

(1) Coronado, E.; Day, P. *Chem. Rev.* **2004**, *104*, 5419−5448.

(2) Maspoch, D.; Ruiz-Molina, D.; Veciana, J. *Chem. Soc. Rev.* **2007**, *36*, 770−818.

(3) Clemente-Leon, M.; Coronado, E.; Marti-Gastaldo, C.; Romero, F. M. *Chem. Soc. Rev.* **2011**, *40*, 473−497.

(4) Rogez, G.; Massobrio, C.; Rabu, P.; Drillon, M. *Chem. Soc. Rev.* **2011**, *40*, 1031−1058.

(5) Tau, A. K. T., Lu, J., Varadan, V. K., Chang, F. K., Tu, J. P., Lam, P. M., Eds.; *Multifunctional Materials and Structures*; Trans Tech Publications: Hong Kong, 2008.

(6) Mukhopadhyay, S. M., Ed.; *Nanoscale Multifunctional Materials: Science and Applications*; Wiley: Hoboken, NJ, 2012.

(7) Halcrow, M. A., Ed.; *Spin-Crossover Materials: Properties and Applications*; John Wiley & Sons: Oxford, U.K., 2013.

(8) Glaser, T. *Chem. Commun.* **2011**, *47*, 116−130.

(9) Holmes, S. M.; Girolami, G. S. *J. Am. Chem. Soc.* **1999**, *121*, 5593−5594.

(10) Miller, J. S. *Chem. Soc. Rev.* **2011**, *40*, 3266−3296.

(11) Bogani, L.; Wernsdorfer, W. *Nat. Mater.* **2008**, *7*, 179−186.

(12) Woodruff, D. N.; Winpenny, R. E. P; Layfield, R. A. *Chem. Rev.* **2013**, *113*, 5110−5148.

(13) Ohkoshi, S.; Tokoro, H.; Matsuda, T.; Takahashi, H.; Irie, H.; Hashimoto, K. *Angew. Chem., Int. Ed.* **2007**, *46*, 3238−3241.

(14) Guo, P.-H.; Liu, J.-L.; Jia, J.-H.; Wang, J.; Guo, F.-S.; Chen, Y.-C.; Lin, W.-Q.; Leng, J.-D.; Bao, D.-H.; Zhang, X.-D.; Luo, J.-H.; Tong, M.-L. *Chem.—Eur. J.* **2013**, *19*, 8769−8773.

(15) Dechambenoit, P.; Long, J. R. *Chem. Soc. Rev.* **2011**, *40*, 3249−3265.

(16) Coronado, E.; Gimenez-Marques, M.; Espallargas, G. M.; Brammer, L. *Nat. Commun.* **2012**, *3*, 828(8).

(17) Kaye, S. S.; Choi, H. J.; Long, J. R. *J. Am. Chem. Soc.* **2008**, *130*, 16921−16925.

DOI: 10.1021/acs.inorgchem.5b00040
Inorg. Chem. 2015, 54, 4724−4736

(18) Chorazy, S.; Nakabayashi, K.; Imoto, K.; Mlynarski, J.; Sieklucka, B.; Ohkoshi, S. *J. Am. Chem. Soc.* **2012**, *134*, 16151−16154.
(19) Train, C.; Gruselle, M.; Verdaguer, M. *Chem. Soc. Rev.* **2011**, *40*, 3297−3312.
(20) Chorazy, S.; Nakabayashi, K.; Ohkoshi, S.; Sieklucka, B. *Chem. Mater.* **2014**, *26*, 4072−4075.
(21) Chelebaeva, E.; Larionova, J.; Guari, Y.; Ferreira, R. A. S.; Carlos, L. D.; Almeida Paz, L. A.; Trifonov, A.; Guerin, C. *Inorg. Chem.* **2009**, *48*, 5983−5995.
(22) Long, J.; Vallat, R.; Ferreira, R. A. S.; Carlos, L. D.; Almeida Paz, F. A.; Guari, Y.; Larionova, J. *Chem. Commun.* **2012**, *48*, 9974−9976.
(23) Yamauchi, S.; Fujinami, T.; Matsumoto, N.; Mochida, N.; Ishida, T.; Sunatsuki, Y.; Watanabe, M.; Tsuchimoto, M.; Coletti, C.; Re, N. *Inorg. Chem.* **2014**, *53*, 5961−5971.
(24) Alberola, A.; Coronado, E.; Galan-Mascaros, J. R.; Gimenez-Saiz, C.; Gomez-Garcia, C. J. *J. Am. Chem. Soc.* **2003**, *125*, 10774−10775.
(25) Hiraga, H.; Miyasaka, H.; Nakata, K.; Kajiwara, T.; Takaishi, S.; Oshima, Y.; Nojiri, H.; Yamashita, M. *Inorg. Chem.* **2007**, *46*, 9661−9671.
(26) Train, C.; Gheorghe, R.; Krstic, V.; Chamoreau, L. M.; Ovanesyan, N. S.; Rikken, G.; Gruselle, M.; Verdaguer, M. *Nat. Mater.* **2008**, *7*, 729−734.
(27) Chorazy, S.; Podgajny, R.; Nitek, W.; Fic, T.; Görlich, E.; Rams, M.; Sieklucka, B. *Chem. Commun.* **2013**, *49*, 6731−6733.
(28) Train, C.; Nuida, T.; Gheorghe, R.; Gruselle, M.; Ohkoshi, S. *J. Am. Chem. Soc.* **2009**, *131*, 16838−16843.
(29) Nuida, T.; Matsuda, T.; Tokoro, H.; Sakurai, S.; Hashimoto, K.; Ohkoshi, S. *J. Am. Chem. Soc.* **2005**, *127*, 11604−11605.
(30) Avendano, C.; Hilfiger, M. G.; Prosvirin, A.; Sanders, C.; Stepien, D.; Dunbar, K. R. *J. Am. Chem. Soc.* **2010**, *132*, 13123−13125.
(31) Pajerowski, D. M.; Gardner, J. E.; Frye, F. A.; Andrus, M. J.; Dumont, M. F.; Knowles, E. S.; Meisel, M. W.; Talham, D. R. *Chem. Mater.* **2011**, *23*, 3045−3053.
(32) Koumousi, E. S.; Jeon, I.-R.; Gao, Q.; Dechambenoit, P.; Woodruff, D. N.; Merzeau, P.; Buisson, L.; Jia, X.; Li, D.; Volatron, F.; Mathoniére, C.; Clérac, R. *J. Am. Chem. Soc.* **2014**, *136*, 15461−15464.
(33) Ohkoshi, S.; Imoto, K.; Tsunobuchi, Y.; Takano, S.; Tokoro, H. *Nat. Chem.* **2011**, *3*, 564−569.
(34) Ohkoshi, S.; Takano, S.; Imoto, K.; Yoshikiyo, M.; Namai, A.; Tokoro, H. *Nat. Photonics* **2014**, *8*, 65−71.
(35) Fernandez, B.; Galvez, N.; Cuesta, R.; Hungria, A. B.; Calvino, J.; Dominguez-Vera, J. M. *Adv. Funct. Mater.* **2008**, *18*, 3931−3935.
(36) Rueff, J.-M.; Nierengarten, J.-F.; Gillor, P.; Demessence, A.; Cregut, O.; Drillon, M.; Rabu, P. *Chem. Mater.* **2004**, *16*, 2933−2937.
(37) Kahn, O.; Larionova, J.; Mathoniére, C.; Sutter, J.-P. *Mol. Cryst. Liq. Cryst.* **1997**, *305*, 1−16.
(38) Ferrando-Soria, J.; Khajavi, H.; Serra-Crespo, P.; Gascon, J.; Kapteijn, F.; Julve, M.; Lloret, F.; Pasán, J.; Ruiz-Pérez, C.; Journaux, Y.; Pardo, E. *Adv. Mater.* **2012**, *24*, 5625−5629.
(39) Sorace, L.; Benelli, C.; Gatteschi, D. *Chem. Soc. Rev.* **2011**, *40*, 3092−3104.
(40) Perrier, M.; Long, J.; Almeida Paz, F. A.; Guari, Y.; Larionova, J. *Inorg. Chem.* **2012**, *51*, 6425−6427.
(41) Bünzli, J-C. G.; Piguet, C. *Chem. Soc. Rev.* **2005**, *34*, 1048−1077.
(42) Przychodzeń, P.; Pełka, R.; Lewiński, K.; Supel, J.; Rams, M.; Tomala, K.; Sieklucka, B. *Inorg. Chem.* **2007**, *46*, 8924−8938.
(43) Chelebaeva, E.; Long, J.; Larionova, J.; Ferreira, R. A. S.; Carlos, L. D.; Almeida Paz, F. A.; Gomes, J. B. R.; Trifonov, A.; Guerin, C.; Guari, Y. *Inorg. Chem.* **2012**, *51*, 9005−9016.
(44) Long, J.; Chelebaeva, E.; Larionova, J.; Guari, Y.; Ferreira, R. A. S.; Carlos, L. D.; Almeida Paz, F. A.; Trifonov, A.; Guerin, C. *Inorg. Chem.* **2011**, *50*, 9924−9926.
(45) Chorazy, S.; Nakabayashi, K.; Ozaki, N.; Pełka, R.; Fic, T.; Mlynarski, J.; Sieklucka, B.; Ohkoshi, S. *RSC Adv.* **2013**, *3*, 1065−1068.
(46) Chorazy, S.; Nakabayashi, K.; Arczynski, M.; Pełka, R.; Ohkoshi, S.; Sieklucka, B. *Chem.—Eur. J.* **2014**, *20*, 7144−7159.
(47) Prins, F.; Pasca, E.; Jos de Jongh, L.; Kooijman, H.; Spek, A. L.; Tanase, S. *Angew. Chem., Int. Ed.* **2007**, *46*, 6081−6084.
(48) Corden, B. J.; Cunningham, J. A.; Eisenberg, R. *Inorg. Chem.* **1970**, *9*, 356−362.
(49) Sheldrick, G. M. *Acta Crystallogr.* **2008**, *A64*, 112−122.
(50) Bain, G. A.; Berry, J. F. *J. Chem. Educ.* **2008**, *85*, 532−536.
(51) Llunell, M.; Casanova, D.; Cirera, J.; Bofill, J.; Alemany, P.; Alvarez, S.; Pinsky, M.; Avnir, D. *SHAPE v. 2.1. Program for the Calculation of Continuous Shape Measures of Polygonal and Polyhedral Molecular Fragments*; University of Barcelona: Barcelona, Spain, 2013.
(52) Casanova, D.; Cirera, J.; Llunell, M.; Alemany, P.; Avnir, D.; Alvarez, S. *J. Am. Chem. Soc.* **2004**, *126*, 1755−1763.
(53) Isci, H.; Roy Mason, W. *Inorg. Chim. Acta* **2004**, *357*, 4065−4072.
(54) Vogler, A.; Kunkely, H. *Inorg. Chim. Acta* **2006**, *359*, 4130−4138.
(55) Herrera, J. M.; Marvaud, V.; Verdaguer, M.; Marrout, J.; Kalisz, M.; Mathoniére, C. *Angew. Chem., Int. Ed.* **2004**, *43*, 5468−5471.
(56) van Pieterson, L.; Reid, M. F.; Burdick, G. W.; Meijerink, A. *Phys. Rev. B* **2002**, *65*, 045114(13).
(57) Chang, Y.-S.; Lin, H.-J.; Li, Y.-C.; Chai, Y.-L.; Tsai, Y.-Y. *J. Solid State Chem.* **2007**, *180*, 3076−3081.
(58) Zhu, X.; Wong, W.-K.; Wong, W.-Y.; Yang, X. *Eur. J. Inorg. Chem.* **2011**, 4651−4674.
(59) Kahn, O. *Molecular Magnetism*; VCH: New York, 1993; pp 43−51.
(60) Carlin, R. C. *Magnetochemistry*; Springer-Verlag: Berlin, 1986; pp 237−261.
(61) Kozieł, M.; Pełka, R.; Rams, M.; Nitek, W.; Sieklucka, B. *Inorg. Chem.* **2010**, *49*, 4268−4277.
(62) Zhou, H.; Diao, G.-W.; Qian, S.-Y.; Yang, X.-Z.; Yuan, A.-H.; Song, Y.; Li, Y.-Z. *Dalton Trans.* **2012**, *41*, 10690−10697.
(63) Zhao, H.; Lopez, N.; Prosvirin, A.; Chifotides, H. T.; Dunbar, K. R. *Dalton Trans.* **2007**, 878−888.
(64) Biradha, K.; Hongo, Y.; Fujita, M. *Angew. Chem., Int. Ed.* **2002**, *41*, 3395−3398.

DOI: 10.1021/acs.inorgchem.5b00040
Inorg. Chem. 2015, 54, 4724−4736